Research Article | Vol. 31, No. 24 / 20 Nov 2023 / Optics Express 40210
Optics EXPRESS

Grazing incidence to total internal reflection fluorescence structured illumination microscopy enabled by a prism telescope

HENNING ORTKRASS,[1,*] GERD WIEBUSCH,[1] JOCHEN LINNENBRÜGGER,[1] JASMIN SCHÜRSTEDT,[1] KAROLINA SZAFRANSKA,[2] PETER MCCOURT,[2] AND THOMAS HUSER[1]

[1]*Biomolecular Photonics Research Group, Faculty of Physics, Bielefeld University, Bielefeld, Germany*
[2]*Department of Medical Biology, UiT - The Arctic University of Norway, Tromsø, Norway*
[*]*hortkrass@physik.uni-bielefeld.de*

Abstract: In super-resolution structured illumination microscopy (SR-SIM) the separation between opposing laser spots in the back focal plane of the objective lens affects the pattern periodicity, and, thus, the resulting spatial resolution. Here, we introduce a novel hexagonal prism telescope which allows us to seamlessly change the separation between parallel laser beams for 3 pairs of beams, simultaneously. Each end of the prism telescope is composed of 6 Littrow prisms, which are custom-ground so they can be grouped together in the form of a tight hexagon. By changing the distance between the hexagons, the beam separation can be adjusted. This allows us to easily control the position of opposing laser spots in the back focal plane and seamlessly adjust the spatial frequency of the resulting interference pattern. This also enables the seamless transition from 2D-SIM to total internal reflection fluorescence (TIRF) excitation using objective lenses with a high numerical aperture. In linear SR-SIM the highest spatial resolution can be achieved for extreme TIRF angles. The prism telescope allows us to investigate how the spatial resolution and contrast depend on the angle of incidence near, at, and beyond the critical angle. We demonstrate this by imaging the cytoskeleton and plasma membrane of liver sinusoidal endothelial cells, which have a characteristic morphology consisting of thousands of small, transcellular pores that can only be observed by super-resolution microscopy.

1. Introduction

Super-resolution structured illumination microscopy (SR-SIM) is a fluorescence-based imaging method that, in its linear implementation, can overcome the diffraction limit by up to a factor of two [1]. This is accomplished by exciting fluorescence in the sample via an interference pattern with a high spatial frequency, which encodes sample information beyond the diffraction limit into the passband of the modulation transfer function of the microscope [2]. Even higher spatial resolution can be achieved by exploiting objective lenses with a high numerical aperture (NA) [3], and by further pushing the spatial frequency of the interference pattern to higher values using counter-propagating evanescent waves generated by total internal reflection fluorescence (TIRF) excitation [4–6]. Li et al. demonstrated that a spatial resolution of down to 84 nm is possible by using a NA1.7 objective lens [3].

When fluorescence is excited by total internal reflection in super-resolution structured illumination microscopy (TIRF-SIM), the interference pattern of standing evanescent waves is created by focusing the interfering laser beams into the back focal plane (BFP) of a high NA microscope objective lens at radii near the edge of the back aperture. In this case the beams encounter the glass-sample interface at an angle beyond the angle of total internal reflection. Near the critical angle, above which total internal reflection takes place, one can distinguish three different special regions that describe how light behaves near the glass-sample interface. For light rays impeding

#504292 https://doi.org/10.1364/OE.504292
Journal © 2023 Received 25 Aug 2023; revised 29 Sep 2023; accepted 2 Oct 2023; published 13 Nov 2023

Optics EXPRESS

the glass-sample interface at angles near the critical angle, the transmitted rays will adopt an angle very close to the glass-sample interface. This region is called "grazing incidence" and, when implemented in SR-SIM, it is called grazing incidence structured illumination microscopy (GI-SIM) [7]. Rays that hit the air-sample interface at the critical angle result in total internal reflection, hence, TIRF-SIM when implemented in SR-SIM. Lastly, for rays that hit this interface at angles much larger than the critical angle we can refer to as the "far TIRF" region, resulting in far TIRF-SIM (fTIRF-SIM).

In current implementations of SR-SIM systems, the illumination pattern is often generated by a spatial light modulator (SLM). These devices offer significant advantages in terms of flexibility in generating the periodicity, angle and phase of the pattern and they can change between patterns with very high speed [8]. Because of the finite pixel dimensions of the SLMs, the patterns required for a specific type of illumination have to be carefully chosen for each illumination wavelength. Finding the proper patterns to cover a wide range of SIM patterns that generate illumination conditions for all wavelengths near the critical angle is difficult, if not even impossible. And each modality will require the use of customized spatial filters that will only let the first diffraction orders pass on to the microscope.

To overcome these issues, several fiber-optics based SR-SIM systems have recently been demonstrated [9–11]. Here, we show how a novel prism telescope allows us to seamlessly change the distance between parallel laser beams focused to the BFP of a high NA objective lens. The radial position of these laser foci in the BFP is directly related to the angle at which the beams will intersect the glass-sample interface. By translating one part of the prism telescope, we can, thus, seamlessly move from GI-SIM to TIRF-SIM to fTIRF-SIM. In this paper we describe the construction and function of this prism telescope, and we investigate how the spatial resolution and the contrast changes as the illumination is moved from GI-SIM to fTIRF-SIM. We demonstrate the versatility of this device by studying how the different conditions affect SR-SIM images of liver sinusoidal endothelial cells (LSECs), in particular their actin network and transmembrane fenestrations, which are a characteristic morphological hallmark of these cells.

2. Results and discussion

2.1. Modified fiber-optic SIM microscope

All measurements were performed with a fiber-optics based SR-SIM microscope [10] that was enhanced by a prism telescope as described in detail below. The optical layout of the SR-SIM microscope is shown in Fig. 1(a). The sample is excited sequentially at 491 nm (100 mW, Cobolt Calypso 100), and at 561 nm (200 mW, Photontec Berlin). The interfering beams are launched to free space from a hexagonal fiber array and focused into the BFP of the objective lens. A custom-manufactured fiber collimator holds all fibers in a hexagonal pattern (angle between pairs of beams: 60°), collimates the beams emitted from every fiber and refocuses the beams individually through the prism telescope to the image plane of a 4f optical relay composed of achromatic lenses (see Fig. 1(a)). The beam foci are then projected by this optical relay into the BFP of the objective lens. The objective lens is a 60x, 1.5 NA (UPLAPO60XOHR, Olympus) with a BFP diameter of approximately 9 mm. The fluorescence is epi-detected through a quad-band dichroic mirror and emission filter (F72-891, AHF) and imaged by a Ploessl-type tube lens (constructed out of 2 Thorlabs Inc. ACT504-500-A achromats) onto a scientific complementary metal-oxide semiconductor camera (sCMOS, pco.edge 4.2).

2.2. Prism telescope

Between the hexagonal holder and the relay telescope we placed a custom-manufactured prism telescope that allows us to continuously adjust the lateral beam position, which is otherwise fixed

Optics EXPRESS

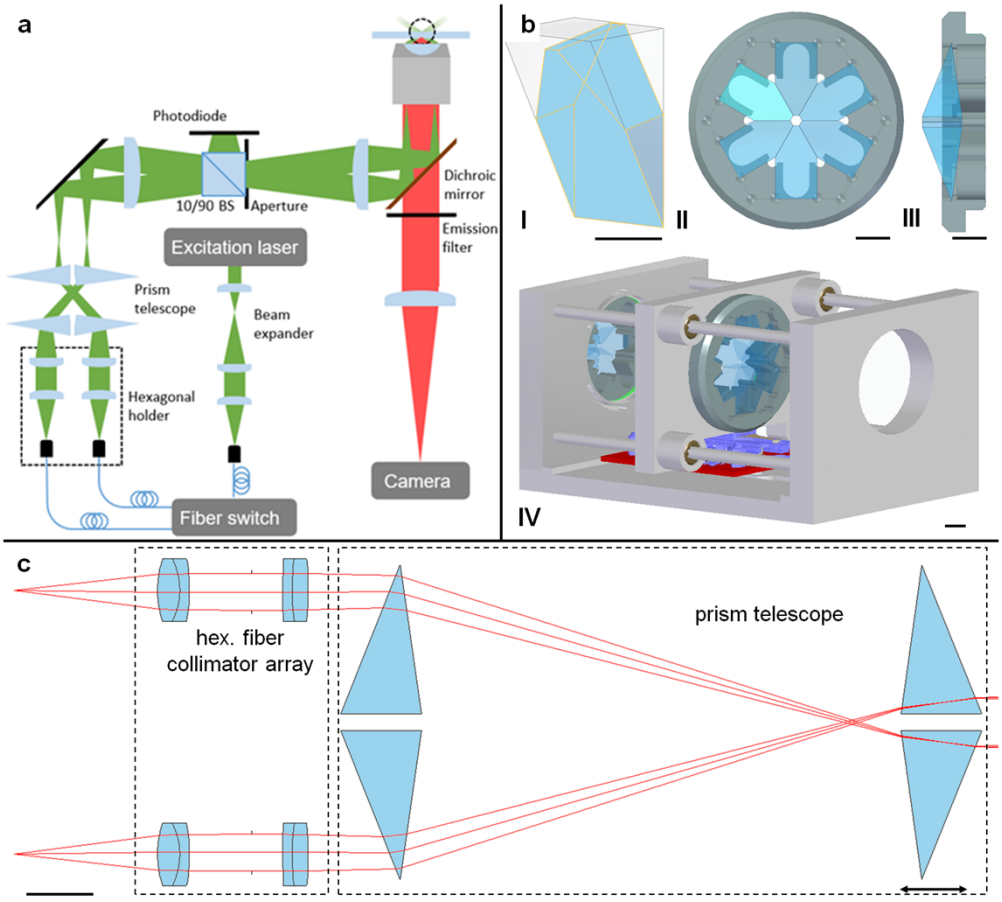

Fig. 1. (a) Schematics of the fiberSIM system as previously published [10], combined with the prism telescope. (bI-bIV) 3D-rendering of a single prism and the assembled hexagonal prism telescope. (bI) Each prism is custom-ground out of a commercial Littrow prism. (bII) The prisms are radially orientated in a hexagonal array and held in a custom-manufactured aluminum frame. (bIII) Side-view of the aluminum frame with prisms. (bIV) Two identical arrays are arranged at opposite ends along the optical axis to form a telescope, where the distance between the prism holders can be varied by a piezo-driven translation stage (ELL17/M, Thorlabs Inc.). (c) This arrangement results in a variable, but symmetric beam displacement of the six off-axis-beams. The beams propagating through the telescope are emitted by six single mode fibers and refocused by a hexagonal fiber collimator array before passing through the prisms. Scale bar is 10 mm (b, c).

Optics EXPRESS

by the hexagonal fiber holder, to a radius smaller than the radius of the BFP. This prism telescope consists of identical pairs of 30°/60°/90° Littrow prisms (along the light propagation axis, see Fig. 1(b),(c)). At each end of the telescope, the prisms are arranged in a hexagonal pattern (array) to allow all beams emerging from the fiber collimator to be displaced evenly by the same amount and to redirect the beams parallel to the optical axis. As shown in Fig. 1(b), each array consists of six radially and symmetrically arranged prisms. The side faces of the upper half of each prism were custom-ground to a triangular shape to allow them to be placed in a tight hexagonal pattern (see Fig. 1(b) II). For each of the six off-axis beams, a first prism (at the front end of the telescope) refracts the incoming beam towards the optical axis and a second prism (at the back end of the telescope) refracts it back to paraxiality (see Fig. 1(c)). The lateral beam position is continuously adjustable by changing the distance between the hexagonal prism arrays.

The two prism arrays are custom-ground out of uncoated Littrow dispersion prisms (Edmund Optics Inc., #43-648) with a size of $12.7 \times 12.7 \times 22\,\mathrm{mm}^3$. They are cut from the sides by 30° and the tip by 8° to allow them to be assembled very closely. The hole in the middle of the prism array has a diameter of 3 mm and allows an on-axis beam to propagate unaffected. This is useful for 3D-SIM or the alignment of consecutive optical elements. The beam distance in the BFP can be adjusted between 6.4 mm (min.) and 40 mm (max.) due to the physical size and custom-manufacturing limitations of the prisms. The adjustable prism array is mounted on stainless steel rods via ball guides and one of the prism holders is actuated by a piezo driven translation stage (ELL17/M, Thorlabs Inc.). The motor and the mechanics allow for a positioning resolution of the spot pattern of 30 µm in the BFP. It typically takes approximately 100 ms to shift between beam displacements of less than 1 mm. See Fig. 1(b) IV for a 3D CAD drawing of the fully assembled and motorized prism telescope.

Since the prisms are passed by converging laser beams, astigmatism induced by the prisms has to be taken into account. In the absence of the prism telescope, the beams are focused in the excitation path of the SIM setup with a cone angle of 40 mrad (at $\frac{1}{e^2}$ intensity). This corresponds to a focus spot diameter of 13 µm (see Fig. 2(a)) for 561 nm excitation light. If the prisms are vertically oriented, such that the beams enter the prism surface tilted by 30° in the Meridional plane, the focus diameter is enlarged and deformed by astigmatism to a size of 40 µm (see Fig. 2(b)). To minimize the astigmatism, the prisms are tilted by 8° in the Meridional plane. We confirmed that this angle indeed best reduces astigmatism by simulating the effect with the optics design software CodeV (Synopsis, Inc.) (see Figs. 2(a)-(c)). This angle can easily be machined with high precision on our department's 5-axis CNC machine. We find that small deviations from this angle of up to 0.5° are insignificant to the proper function of the prism telescope. Due to this 8° tilt, the beams enter the prisms through a 22° tilted surface and exit them through a -8° tilted surface. The measured focus diameter is 15 µm (see Fig. 2(c) and 2(d)). We find the aberrations to not be wavelength dependent within the limits of the laser sources available to us. A diffraction limited focus diameter is necessary in order to obtain a homogenous sinusoidal interference pattern in the sample plane. The observed sinusoidal pattern displays a symmetric Gaussian intensity distribution and a modulation contrast of >82% over the entire field of view (FOV) of up to 150 µm as measured with the fairSIM imageJ plugin [12], allowing SR-SIM image reconstructions without having to tile the raw data.

The radial beam position depends linearly on the separation between the prisms. The beams are tilted by 16.3° in the space between the prisms (see Fig. 1(c)). We confirmed that the paraxiality of the beams as well as their azimuthal position after passing the prisms is maintained over the full travel range of the prisms. This allows us to seamless tune the setup from generating a coarse 2D-SIM pattern, through grazing incidence near the critical angle, and all the way to the TIRF limit of the objective lens without reducing the quality of the sinusoidal interference pattern. This is shown for three select spot patterns in the BFP in Fig. 2(d). Here, the spot pattern in the BFP for angles at the glass-sample interface of 63°, 72° and 81° were imaged and overlaid. Colored

Optics EXPRESS

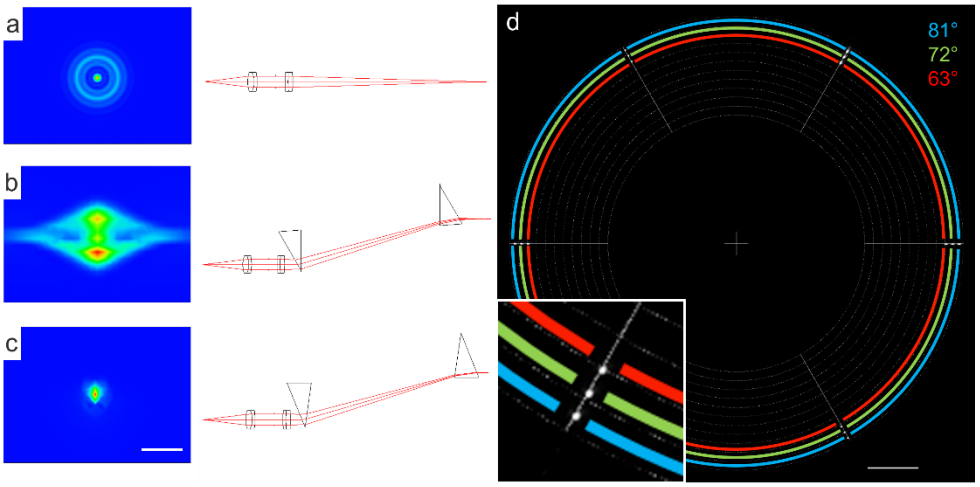

Fig. 2. (a-c) Beam synthesis propagation and ray tracing simulation using the optics design software CodeV for different optical configurations of the prism telescope. a) Without the prism telescope, the refocused beam from the fiber is diffraction limited in the BFP with a diameter of 13 µm. b) With an uncompensated prism telescope, significant astigmatism occurs, the diameter is increased to 40 µm. c) By tilting the prisms by 8°, the astigmatism can be minimized, the focus diameter is 15 µm. The aberrations are not wavelength dependent. By axially shifting the second prisms, the beam displacement can be seamlessly tuned. d) Image of the back focal plane of the objective lens. The inset in the lower left hand corner shows an enlarged view of the lower left beam foci. This image is the superposition of three images with laser spot locations highlighted by the colored ring diameters, which indicate the foci position for GI (red), TIRF (green) and the upper TIRF limit (blue). The thin white cross and lines are generated by a Python script during the acquisition and display of the camera frames and indicate the position of the optical axis (cross) and the lines along which the spots should move in order to achieve the three SR-SIM angles. Scale bar is 100 µm (a-c) and 1 mm (d).

circles (red: 63°, green: 72°, blue: 81°) indicate the rings in the BFP for the corresponding angles. The thin white lines shown in the figure are generated by a Python script during display of the BFP camera data and are used as guides to the eye during alignment. The axial focus position varies for different beam distances in the BFP due to different optical path lengths in the prism telescope. For beam distances corresponding to 2D-SIM and far TIRF-SIM, the focus shifts axially by 0.5 mm in the BFP. This does, however, not distort the excitation pattern or the Gaussian intensity distribution nor does it affect TIRF imaging.

Since the angle of refraction in between the prisms slightly depends on the wavelength of the excitation laser beams, the prism distance needs to be adjusted for each excitation wavelength in order to maintain a certain radial beam position for the different wavelengths. For example, for a wavelength of 647 nm the separation between the prism needs to be 1.3 mm larger than for 488 nm to obtain the same separation between the beams.

2.3. Sample preparation

The first step of sample preparation is coating the #1.5 coverglass slides with fibronectin to improve cell adhesion. To accomplish this, the 25 mm diameter cover glass slides are incubated in fibronectin (0.2 mg ml^{-1} in Phosphate Buffered Saline (PBS)) for 45 minutes at room temperature and are washed with PBS afterwards. The cryopreserved rat LSECs are prepared as described previously [13]. The cells were thawed at 37°C until nearly all ice inside the vial is gone. The

Optics EXPRESS

cells were gently pipetted to 24 ml of prewarmed RPMI 1640 media. The cell suspension was centrifuged at 50 g for 3 minutes to remove any other remaining cell types after LSEC separation e.g. hepatocytes. The supernatant containing the LSECs was used for a second centrifugation step at 300 g for 8 minutes. The cell pellet is then resuspended in 10 ml fresh RPMI 1640 media. A volume of 1.5 ml of cell suspension is added to each coated coverglass, resulting in a density of 100.000 cells per cm^2. After 1 hour in the incubator at 37°C and 5% CO_2, the cells are washed with new media and placed in the incubator for another 2 hours.

Subsequently, the LSECs were fixed with 4% paraformaldehyde in PBS for 10 minutes and washed three times with PBS before staining. The membrane of the cells was stained with a 1:200 dilution of BioTracker 555 Orange Cytoplasmic Membrane Dye (SCT107, Sigma-Aldrich) in PBS for 1 hour at room temperature. In addition, the actin cytoskeleton was stained with 1:40 Alexa Fluor 488 Phalloidin (A12379, ThermoFisher) in PBS for 2 hours at room temperature without prior permeabilization. All SR-SIM experiments of the fixed and stained cells were conducted in PBS.

2.4. Theoretical considerations about the resolution enhancement in TIRF-SIM

In SR-SIM the angle of incidence (AOI) at the glass (cover slip) - sample interface and the resulting spatial frequency of the interference pattern is adjusted by shifting the radial position of the beam foci in the back focal plane (BFP) of the objective lens. The radius of the beam focus r in the BFP with regard to the Abbe sine condition is proportional to the sine of the angle θ of the beam exiting the objective lens [14]:

$$r \propto \sin\theta$$

The separation between two maxima of the interference pattern (pattern spacing) s in the sample plane is given by:

$$s = \frac{\lambda}{2n\sin\theta},$$

where λ is the laser wavelength and n is the refractive index of the cover glass. The AOI θ can therefore be calculated by the pattern frequency $k = \frac{1}{s}$ obtained from the image:

$$\theta = \sin^{-1}\frac{\lambda k}{2n}$$

The critical angle $\theta_{critical}$ for total internal reflection (TIR) is given by the ratio of the refractive indices (RI) of the media comprising the interface. For cells, the refractive index of the plasma membrane is between 1.46 and 1.54 [15], whereas the RI of the cytoplasm in living cells is approximately 1.38 [16]. In fixed and mounted cells, the refractive index of the cytoplasm changes due to the presence of the embedding medium to values between 1.33 and 1.38. Due to the thickness of the cell's plasma membrane, i.e. typically less than 13 nm [17], the effect of the membrane itself can be neglected [18]. In this case the TIR condition can be calculated by the refractive index of the cover glass ($n_1 = 1.518$) and the cytoplasm ($n_2 = 1.33 \ldots 1.38$). The critical angle is therefore:

$$\theta_{critical} = \sin^{-1}\frac{n_2}{n_1} = 61.2^\circ \ldots 65.4^\circ$$

The maximum acceptance angle of the objective lens θ_{max} is limited by the NA of the objective lens (in our experiments a 60x Olympus UPLAPO60XOHR, NA = 1.50, is used):

$$\theta_{max} = \sin^{-1}\frac{n_1}{NA} = 81.2^\circ$$

Optics EXPRESS

The intensity of the evanescent field at the glass-cell interface for s-polarized beams also varies depending on θ and is [19]:

$$I_0 = \frac{4\,|A_s|^2 \cos\theta^2}{1 - \frac{n_2^2}{n_1^2}}$$

where A_s is the electric field amplitude of the s-polarized laser beam. The illumination intensity thus decreases with increasing illumination angles as shown by the blue curve in Fig. 3(a).

The theoretically achievable improvement in spatial resolution d by SR-SIM depends on the Abbe resolution limit $d_{detection}$ and the pattern spacing s:

$$\begin{aligned} d &= \frac{d_{detection}}{s} + 1 \\ &= \frac{\frac{\lambda_{em}}{2n}}{\frac{\lambda_{ex}}{2NA\sin\theta}} + 1 \\ &= \frac{\lambda_{em} n \sin\theta}{\lambda_{ex} NA} + 1 \end{aligned}$$

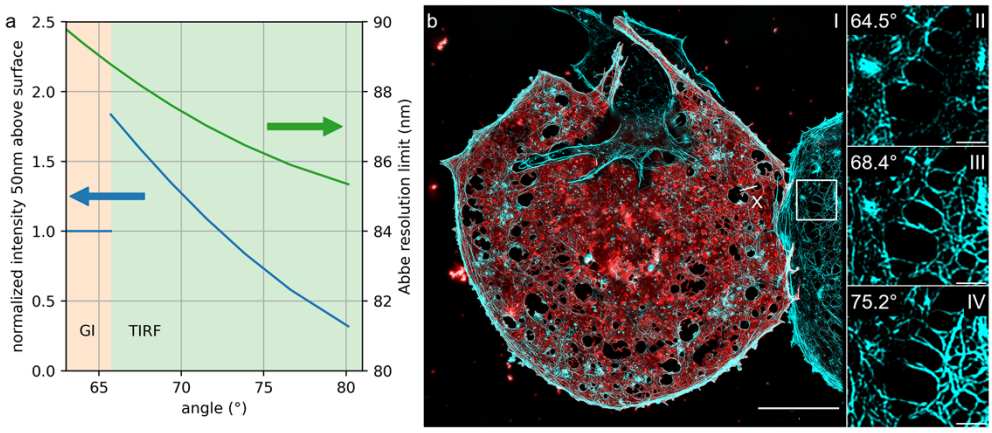

Fig. 3. a) The theoretical resolution limit for SR-SIM (using the Abbe condition) dependent on the excitation angle (green curve); as well as the normalized TIRF and GI excitation intensity 50 nm above the coverslip-sample interface (blue curve). b) TIRF-SIM image of rat LECs stained with phalloidin-AF 488 against actin and BioTracker 555 Orange against the plasma membrane (Panel I). The cell imaged only partially on the right hand side did not take up any membrane stain. The image is an average of 16 reconstructed images per channel, acquired with different GI and TIRF angles between 63.3° and 80.1°. The thin white line marked by "X" indicates the cross sections shown in Fig. 4(c). Panels II-IV show the actin cytoskeleton for GI excitation corresponding to an angle of 64.5° (II) and TIRF excitation with angles of 68.4° (III), 75.2° (IV). Scale bar is 10 μm (Panel I) and 1 μm (Panels II-IV).

For an excitation wavelength of λ_{ex} =488 nm and a fluorescence emission wavelength centered at λ_{em} = 530 nm, the critical angle and the maximum acceptance angle of the objective lens correspond to resolution improvements between d = 1.95 and d = 1.99, and up to d = 2.07. The intensity of the evanescent field and the Abbe limit of the maximum spatial resolution that can be obtained by linear SR-SIM are shown in Fig. 3(a). Prior to reaching the critical angle the intensity of the laser illumination is not affected by the illumination angle and was normalized to 1. This value then suddenly increases at the critical angle due to the limited penetration depth of the electric field into the lower index medium and rapidly decreases with the cosine-squared of the angle of illumination.

Optics EXPRESS

2.5. GI-SIM and TIRF-SIM imaging of biological samples

We next explored the ability of our prism telescope enhanced fiberSIM system to image biological samples by GI-SIM and TIRF-SIM using different excitation pattern spacings. Fluorescently stained actin filaments in fixed LSECs were imaged at 16 different angles near the critical angle between the glass-sample interface ranging from 63.3° to 80.1°. Figure 3(b) shows a two-color SR-SIM image of LSECs, where actin filaments are displayed in blue and the plasma membrane is overlayed in red. This image is an average of the 16 SR-SIM images that were reconstructed for each color channel and, thus, contains information obtained from all illumination angles. The image shows a doubly stained LSEC in full in the center of the image. The membrane staining of the cells located on top and on the right side of the image is not visible due to the contrast adjustments to emphasize the details visible in the central LSEC. The difference in the intensity of the LSEC membrane staining using the BioTracker stain is not fully understood. According to the manufacturer the dye is sensitive to the disruption of the cell membrane which could have been affected by the individual cell viability prior to fixation, fixation artefacts or the order of staining (the actin cytoskeleton was stained in the first step).

The cell in the center exhibits several large gaps (several 100 nm to microns in diameter) in its plasma membrane, but it also contains a significant number of small holes with diameters on the order of 100 nm (some of which can be seen more clearly in the insets to Fig. 5). These small holes are fenestrations, the main morphological hallmark of LSECs. As can be seen in Fig. 3 and in more detail in Fig. 5, all of these transmembrane holes are surrounded by actin fibers. Actin fibers also provide the main link of the circumference of the cells to the substrate. In addition, several focal adhesions, where actin fibers inside the cell bundle up and connect the cell to the substrate can also be identified. Panels II-IV in Fig. 3(b) show the actin cytoskeleton for TIRF excitation corresponding to angles of 64.5° (GI-SIM, Panel II), 68.4° (TIRF-SIM, Panel III) and 75.2° (fTIRF-SIM, Panel IV). The angles result in different illumination pattern spacings as well as different decay lengths of the evanescent field in axial direction, which explains why different parts of the actin cytoskeleton are visible in these images, also noticeable in Fig. 5. This angle-dependent change in contrast offers interesting potential for 3D imaging of thin cells. We are currently investigating this aspect in more detail and plan to report on it in a separate publication.

Next, we systematically evaluated the spatial resolution that can be obtained by the different illumination angles for the actin channel (488 nm excitation wavelength, 100 ms exposure time, $< 25 W/cm^2$). In order to obtain quantitative information about the spatial resolution, two subsequently acquired SR-SIM images taken at the same illumination angle were analyzed by Fourier ring correlation (FRC) using an ImageJ plugin [20]. As can be seen from Fig. 4(a), the spatial resolution improves from 100.8 nm for grazing incidence to 97.9 nm at the TIRF angle and reaches a plateau at 95.8 nm for an fTIRF angle of 75°, corresponding to a resolution improvement of 2.07x over conventional widefield fluorescence microscopy. For angles beyond this value, the signal-to-noise ratio (SNR) of the images deteriorates due to the dependence of the intensity of the illumination, which causes the FRC-measured spatial resolution to increase, again. Figure 4(b) shows the FRC curves for several select angles. The experimentally determined spatial resolution follows a similar curve as the theoretical prediction in Fig. 3(a), and rapidly improves with increasing angle. The theoretical resolution predicted by the Abbe criterion can, however, not be reached experimentally due to the various aberrations encountered in real optical systems. To determine if the resolution continues to improve beyond an angle of approx. 72° would require to either adjust the excitation power or extend the acquisition time for images taken at such extreme angles in order to improve their SNR.

We also evaluated qualitatively how the image contrast behaves for angles before and beyond the critical angle. The result is shown in Fig. 4(c) in the form of cross sections through several actin fibers that were taken from images consecutively obtained at a GI excitation angle (63.3°, green),

Optics EXPRESS

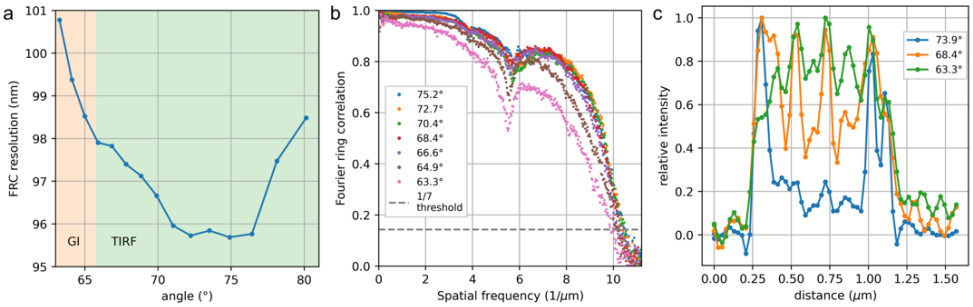

Fig. 4. a) Spatial resolution obtained across the entire reconstructed image as measured by Fourier ring correlation (FRC). The curve indicates that the lateral resolution continues to improve with increasing illumination angles until the SNR limits the resolution, due to the simultaneously decreasing excitation intensity. b) FRC curves for several select angles. The values at the 1/7 threshold are plotted in a). c) Lineplots through several actin fibers lying in close proximity from images obtained at GI excitation angle (63.3°, green), the TIRF angle (68.4°, orange) and an far TIRF angle (73.9°, blue).

the TIRF angle (68.4°, orange) and an fTIRF angle (73.9°, blue). The cross sections are taken at the same position in the reconstructed images and were normalized to the background. As can be seen by this graph, while the overall signal to background level is similar for the different angles, different actin fibers are emphasized at different angles and the overall signal-to-background ratio continuously improves with increasing excitation angle.

To further demonstrate how spatial resolution and image contrast change with increasing illumination angle, Fig. 5 shows select SR-SIM images of the rat LSECs shown in the overlay in Fig. 3(b) for different GI and TIRF angles. The upper row shows the actin channel, while the lower row shows the plasma membrane channel. The spatial resolution as determined by FRC ranges from 103 nm - 98 nm for the actin channel and 115 nm - 111 nm for the membrane channel. While contrast and spatial resolution do not visibly change between the different plasma membrane images, a very different effect can be seen in the actin channel. Here, depending on the illumination angle, different actin fibers begin to become visible, as is most apparent by the change in brightness of the actin filaments in the outer circumference of the cells. The change in contrast in the actin channels shown in the insets to Fig. 5(b) and 5(c) is minute, which is most likely due to the overall very small thickness of these parts near the circumference of the cell of just about 300 nm and the actin skeleton being concentrated mostly near the glass surface. This can be best explained by changes in the penetration depth of the evanescent field and this effect has previously been exploited in order to improve the axial resolution of TIRF-SIM images, albeit so far only by varying the angle for TIRF illumination and not with the corresponding SIM pattern [21].

Optics EXPRESS

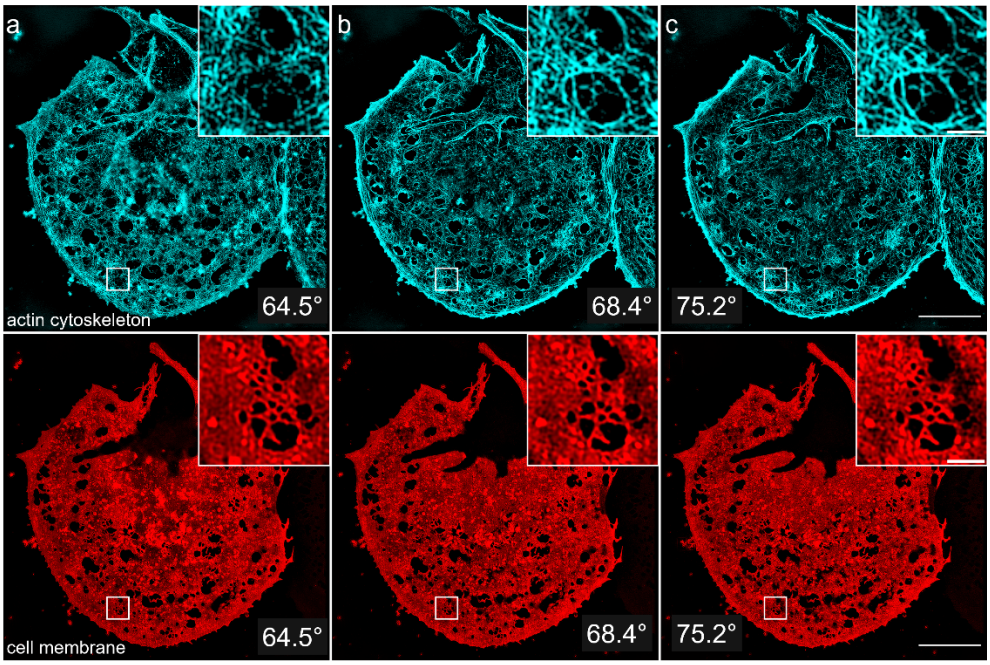

Fig. 5. TIRF-SIM image of the rat liver endothelial cells shown in Fig. 3 for different TIRF and GI angles. The upper row shows the actin channel, while the lower row shows the plasma membrane channel. a) The actin and membrane channels have a FRC resolution of 103 nm (actin) and 115 nm (membrane) for an excitation angle of 64.5°, i.e. GI excitation. b) At the TIRF angle (68.4°) the FRC resolution is 98 nm (actin) and 114 nm (membrane). c) For the far TIRF angle of 75.2°, the FRC resolution is 99 nm (actin) and 111 nm (membrane). Scale bar is 10 µm (1 µm in inset).

3. Conclusion

We have introduced a novel prism-based telescope, which allows us to continuously vary the excitation angle of SR-SIM illumination pattern. This is accomplished by translating the separation between corresponding pairs of prisms along the optical axis. By using a piezo-actuated translation stage, fine and continuous adjustments as well as rapid changes in the separation of the resulting laser spots in the back focal plane of an objective lens can be achieved. This enables us to continuously vary the SR-SIM excitation from objective-type grazing incidence to TIRF-SIM excitation and allows us to reach far TIRF-SIM angles. We have evaluated the spatial resolution and the changes in contrast provided by these different illumination modalities and find that the spatial resolution continues to improve up to an illumination angle of approx. 75°. Because of the simultaneously occurring decrease in the illumination power at such extreme angles, the SNR for images obtained beyond an excitation angle of 75° is so low, that the spatial resolution appears to decline, again. To compensate for this effect, the excitation laser power or signal accumulation times would have to be adjusted, which complicates the quantitative comparison of data acquired at these different angles.

Funding. Universitätsbibliothek Bielefeld (Open Access Publication Fund); European Regional Development Fund (NRW - patent validation); HORIZON EUROPE European Innovation Council (101046928).

Acknowledgments. Funding for this project was provided by the European Regional Development Fund 2014 - 2020 programme “NRW-patent validation” under the project “Fiber-SIM”. This project has also received funding from the European Union’s European Innovation Council PATHFINDER Open Programme under grant agreement No

Optics EXPRESS

101046928. We acknowledge support for publication costs by the Open Access Publication Fund of Bielefeld University and the Deutsche Forschungsgemeinschaft (DFG). We thank Dr. Wolfgang Hübner for his guidance and input related to proper LSEC fluorescence staining.

Disclosures. TH and GW submitted a patent application related to fiberSIM through their employer (Bielefeld University). The other authors declare no conflicts of interest.

Data availability. Data underlying the results presented in this paper are not publicly available at this time but may be obtained from the authors upon reasonable request.

References

1. M. G. Gustafsson, "Surpassing the lateral resolution limit by a factor of two using structured illumination microscopy," J. Microsc. **198**(Pt 2), 82–87 (2000).
2. R. Heintzmann and T. Huser, "Super-Resolution Structured Illumination Microscopy," Chem. Rev. **117**(23), 13890–13908 (2017).
3. D. Li, L. Shao, B.-C. Chen, X. Zhang, M. Zhang, B. Moses, D. E. Milkie, J. R. Beach, J. A. Hammer, M. Pasham, T. Kirchhausen, M. A. Baird, M. W. Davidson, P. Xu, and E. Betzig, "Extended-resolution structured illumination imaging of endocytic and cytoskeletal dynamics," Science **349**(6251), aab3500 (2015).
4. P. Kner, B. B. Chhun, E. R. Griffis, L. Winoto, and M. G. L. Gustafsson, "Super-resolution video microscopy of live cells by structured illumination," Nat. Methods **6**(5), 339–342 (2009).
5. E. Chung, D. Kim, and P. T. So, "Extended resolution wide-field optical imaging: objective-launched standing-wave total internal reflection fluorescence microscopy," Opt. Lett. **31**(7), 945–947 (2006).
6. G. E. Cragg and P. T. C. So, "Lateral resolution enhancement with standing evanescent waves," Opt. Lett. **25**(1), 46–48 (2000).
7. Y. Guo, D. Li, S. Zhang, Y. Yang, J.-J. Liu, X. Wang, C. Liu, D. E. Milkie, R. P. Moore, U. S. Tulu, D. P. Kiehart, J. Hu, J. Lippincott-Schwartz, E. Betzig, and D. Li, "Visualizing Intracellular Organelle and Cytoskeletal Interactions at Nanoscale Resolution on Millisecond Timescales," Cell **175**(5), 1430–1442.e17 (2018).
8. A. Markwirth, M. Lachetta, V. Mönkemöller, R. Heintzmann, W. Hübner, T. Huser, and M. Müller, "Video-rate multi-color structured illumination microscopy with simultaneous real-time reconstruction," Nat. Commun. **10**(1), 4315 (2019).
9. J. Pospíšil, G. Wiebusch, K. Fliegel, M. Klíma, and T. Huser, "Highly compact and cost-effective 2-beam super-resolution structured illumination microscope based on all-fiber optic components," Opt. Express **29**(8), 11833 (2021).
10. H. Ortkrass, J. Schürstedt, G. Wiebusch, K. Szafranska, P. McCourt, and T. Huser, "High-speed TIRF and 2D super-resolution structured illumination microscopy with large field of view based on fiber optic components," Opt. Express **31**(18), 29156 (2023).
11. T. A. Hinsdale, S. Stallinga, and B. Rieger, "High-speed multicolor structured illumination microscopy using a hexagonal single mode fiber array," Biomed. Opt. Express **12**(2), 1181–1194 (2021).
12. M. Müller, V. Mönkemöller, S. Hennig, W. Hübner, and T. Huser, "Open-source image reconstruction of super-resolution structured illumination microscopy data in ImageJ," Nat. Commun. **7**(1), 10980 (2016).
13. V. Mönkemöller, H. Mao, W. Hübner, G. Dumitriu, P. Heimann, G. Levy, T. Huser, B. Kaltschmidt, C. Kaltschmidt, and C. I. Øie, "Primary rat LSECs preserve their characteristic phenotype after cryopreservation," Sci. Rep. **8**(1), 14657 (2018).
14. E. Abbe Hon, "VII.—On the Estimation of Aperture in the Microscope," J. R. Microsc. Soc. **1**(3), 388–423 (1881).
15. R. Barer and S. Joseph, "Refractometry of Living Cells," (n.d.).
16. K. F. A. Ross, "Measurement of the Refractive Index of Cytoplasmic Inclusions in Living Cells by the Interference Microscope," Nature **174**(4435), 836–837 (1954).
17. R. A. Meyer, "Light scattering from biological cells: dependence of backscatter radiation on membrane thickness and refractive index," Appl. Opt. **18**(5), 585–588 (1979).
18. D. Axelrod, "Chapter 7: Total internal reflection fluorescence microscopy," Methods Cell Biol. **89**, 169–221 (2008).
19. Y. Fu, P. W. Winter, R. Rojas, V. Wang, M. McAuliffe, and G. H. Patterson, "Axial superresolution via multiangle TIRF microscopy with sequential imaging and photobleaching," Proc. Natl. Acad. Sci. U. S. A. **113**(16), 4368–4373 (2016).
20. N. Banterle, K. H. Bui, E. A. Lemke, and M. Beck, "Fourier ring correlation as a resolution criterion for super-resolution microscopy," J. Struct. Biol. **183**(3), 363–367 (2013).
21. Y. Chen, W. Liu, Z. Zhang, C. Zheng, Y. Huang, R. Cao, D. Zhu, L. Xu, M. Zhang, Y.-H. Zhang, J. Fan, L. Jin, Y. Xu, C. Kuang, and X. Liu, "Multi-color live-cell super-resolution volume imaging with multi-angle interference microscopy," Nat. Commun. **9**(1), 4818 (2018).